Improving g-C_3N_4:WO_3 Z-Scheme Photocatalytic Performance under Visible Light by Multivariate Optimization of g-C_3N_4 synthesis

Fellipe Magioli Cadan*[a], Caue Ribeiro[b], and Eduardo Bessa Azevedo[a]

[a]Department of Molecular Chemistry and Physics, São Carlos Chemistry Institute, São Paulo University. Trabalhador São-Carlense Avenue – 400, São Carlos, Brazil. +55 3373–9978, fellipecadan@usp.br

[b]National Nanotechnology Laboratory for Agriculture, Brazilian Agriculture Research Corporation (Embrapa). XV de Novembro Street – 1452, São Carlos, Brazil.

ABSTRACT

This study reports the optimization of the g-C_3N_4 synthesis by the melamine-annealing route using the Response Surface Methodology (RSM) and its direct coupling to WO_3 by a simple sono-assisted synthesis of g-C_3N_4:WO_3 heterojunctions, with good materials homogenization, effective interface, and proper energy levels. The optimized synthetic conditions were: 605°C, 183 min, and 5°C min^{-1}, producing a high-quality material in comparison with the ones reported in papers published between 2016-2020, as far as bandgap energies and specific surface areas are concerned (SSA/Eg ratio). The highest photocatalytic activity was observed in the 80:20 (wt.%) heterostructure. That material presented a high visible response, being capable of completely degrading the model-pollutant approximately four times faster than g-C_3N_4. The efficient flux of photo-generated electrons though a Z-Scheme heterojunction promoted a superior superoxide radical formation, resulting in increased pollutant degradation. Finally, a complete mechanism for the heterostructure photocatalysis was proposed based on theoretical and experimental results.

KEYWORDS: g-C_3N_4; WO_3; RSM; Z-scheme; photocatalysis

1. INTRODUCTION

Solar-driven photocatalysis has been investigated over the last years as a prospective method for water decontamination, but the lack of efficient catalysts under visible light limits its application on a large scale [1]. Recently, graphitic carbon nitride (g-C_3N_4), a semiconductor polymer composed of heptazine rings (tri-*s*-triazine), was shown to be a promising photocatalyst due to its low bandgap, as well as its very simple preparation compared to other similar semiconductors [2,3]. Nevertheless, the photocatalytic activity of bulk g-C_3N_4 is lower than that of classical materials (e.g. TiO_2) due to the fast recombination rate of the generated charge carriers, poor crystallinity, and relative small specific surface area [3].

Typically, g-C_3N_4 is synthesized by calcination of *n-triazinic* compounds, especially melamine, which is structurally similar to g-C_3N_4 and possibly provides the closest structural precursor. This simple synthesis has efficiencies higher than 20% wt, making it economically attractive [4,5]. However, there is no consensus regarding the initial solid-phase synthesis conditions, which could result in different photocatalytic activities [6,7]. To the best of our knowledge, those optimized annealing conditions have not been defined yet, leading to several discrepancies among similar reports.

Similarly, tungsten trioxide (WO_3) is a key material in a variety of areas, i.e., solar panels, superconductor devices, and heterogeneous photocatalysis [8]. WO_3 has non-stoichiometric properties as a result of oxygen defects and can be synthesized in at least three common crystallographic phases [9]. Those facts generate a broad range of possible bandgaps, from 2.4 to 2.8 eV [10,11]. Although those bandgaps are within the visible region of the electromagnetic spectrum, the energy levels of WO_3 may not be capable of promoting some desirable photo-induced reactions, like superoxide radical formation. Usually, WO_3 synthesis follows standard methodologies for regular oxides, such as: simple annealing [12], sol-gel [13], acidic precipitation [14], hydro- and solvothermal [15,16], etc. Recent studies reported proper photocatalytic properties of sonochemically-synthesized WO_3 [17]. Although its simplicity and relatively low cost, as far as we know, it lacks information about that route in the literature.

The literature points out that the limitations of those two materials could be overcome if they were combined with each other [18–20]. Fast recombination (in g-C_3N_4) and absence of proper energy levels (in WO_3) are reduced by type-II or Z-Scheme heterojunctions. In both alternatives, electrons can be physically separated from holes, promoting redox reactions that cannot take place with the isolated materials. The g-C_3N_4/WO_3 heterostructure has typically been prepared by the simple impregnation of bulk pre-formed photocatalysts [17,18,20]. Although that methodology generates improved photocatalysts, it could lead to materials with low homogeneity and ineffective interfaces. Unfortunately, non-optimized synthetic conditions may generate materials with features not suited for the desired application. Therefore, a new synthetic route capable of overcoming both limitations is needed.

This work initially optimizes the g-C_3N_4 synthesis (annealing method) by the response surface methodology (RSM) [21]. Three parameters were studied: annealing temperature (AT) and time (At), and heating rate (HR). The resulting photocatalyst was directly incorporated into the sono-assisted WO_3 synthesis, yielding a new and simple route for obtaining g-C_3N_4/WO_3 heterostructures. The sono-assisted synthesis of metal oxides has been used, especially for synthesizing TiO_2 and ZnO, mostly for making it possible their formation in shorter times, under mild conditions [22,23]. Finally, several characterization techniques were performed, to gain a better understanding of which structural and/or surface factors were significant to the enhanced photocatalytic activity.

2. MATERIALS AND METHODS

2.1. g-C_3N_4 Synthesis Optimization

Initially, a full 2^3 factorial design (FFD, three factors, two levels) was performed to obtain preliminary information about the effect of each parameter on the chosen response-variable (photocatalytic activity). Three factors were studied: annealing temperature (AT, 500 and 600ºC), annealing time (At, 120 and 180 min), and heating rate (HR, 5 and 10ºC min^{-1}). The 16 experiments were randomly performed with genuine replicates. Table S1 shows the experimental matrix, with real and coded factors.

Next, a series of experiments were performed along the path of the steepest ascent of the surface defined by the FFD results until a local maximum was achieved (Table S2). A central composite design (CCD) was then performed using that local maximum as the central point. Table S3 presents studied factors, levels, and the experimental matrix. A polynomial model was adjusted to the obtained responses and the global maximum was estimated. The model adjustment was evaluated by an analysis of variance (ANOVA) and validation experiments (Table S4 and Table S5).

The solid-phase synthesis was based on the melamine precursor (Sigma-Aldrich, 99%). Typically, 2 g of melamine was added to a semi-closed alumina crucible (Chiarotti, A-45) and treated at the established conditions described in the experimental matrix. Annealing was performed in an EDG 7000 muffle, coupled with an EDG EDGCON 3P heater. The crucible was positioned in the center of the muffle.

2.2. Sono-assisted g-C_3N_4/WO_3 Heterostructures Preparation

A series of g-C_3N_4/WO_3 heterostructures were obtained (CN20 – CN80, meaning 20 to 80%wt of the synthesized g-C_3N_4). The steps taken to prepare those heterostructures are shown in Figure 1.

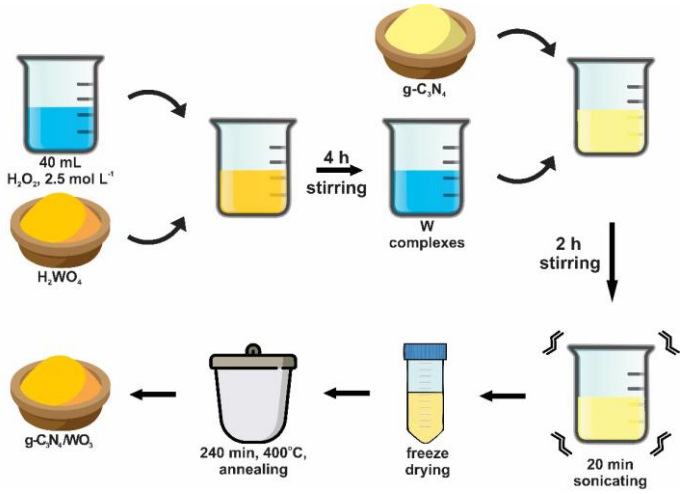

Figure 1. Proposed sono-assisted synthetic route for g-C_3N_4/WO_3 heterostructures.

Typically, a certain mass of H_2WO_4 was suspended in a beaker containing 40 mL of H_2O_2 2.5 mol L^{-1}, forming a yolk-yellow suspension. That suspension was magnetically stirred until the formation of peroxo-tungsten complexes took place (approximately 4 h). The total conversion was clearly noticed when the suspension turned into a colorless solution. A variable amount of g-C_3N_4 was then added to the beaker. The resulting suspension was magnetically stirred for 2 h.

The suspension was then sonicated in a Branson Digital Sonifier 450 (400 W, 20% amplitude) for 20 min (the beaker was kept immersed in an ice bath), transferred to a Falcon tube (50 mL), and freeze-dried. The remaining powder was annealed in an EDG 7000 muffle, coupled with an EDG EDGCON 3P heater (10°C min^{-1}) for 4 h at 400°C. The product was ground in an agate mortar/pestle and stored in amber flasks. The same procedure was repeated twice, with just one of the precursors at a time, for obtaining control samples (CN0 and CN100 for WO_3 and g-C_3N_4, respectively).

2.3. Photocatalytic Activity Assessment

The reaction was carried out in a 250-mL jacketed Pyrex® open reactor containing the suspension (50 mL) with the model-pollutant solution (tartrazine, 25 mg L^{-1}) and the synthesized material under stirring. For experiments in the visible range, a

medium-pressure Hg lamp (Philips HPL-N, 250 W) was positioned 15 cm above the surface of the suspension. For UV-Vis experiments, the same conditions were used, except for the lamp had its outer bulb removed (optimization experiments).

Typically, the suspensions (25 mg) were irradiated for 30 min at 20°C, with 250 mL min^{-1} air bubbling, and magnetic stirring. Afterward, the suspensions were vacuum-filtered (0.45 μm) and the remaining tartrazine concentration was determined by high performance liquid chromatography coupled to a diode array detector (HPLC-DAD). The chromatographic conditions were: Agilent ZORBAX SB-C18 column, 30°C, 1 mL min^{-1} flow rate, 427 nm. The mobile phase gradient was (A, acetate buffer at pH 4; B, methanol): 10% B from 0 to 2 min; then, 10–60% B in 2–4 min; 60% B from 4 to 8 min; 60–10% B in 8–10 min. Control experiments under nearly identical conditions, but without photocatalyst (direct photolysis) and without illumination (dark adsorption) were also performed.

The photocatalyst recyclability was assessed in the same conditions of the photocatalytic activity tests, except for using the same mass of semiconductor several times. After each batch experiment (30 min), the photocatalyst was vacuum-filtered in a 0.45 μm cellulose membrane. The retained solid was recovered (by removing the solid of the membrane with a gentle flux of the next pollutant solution) directly to the next batch. By doing so, approximately the same mass of the photocatalyst could be recovered, repeatedly.

2.4. Optical and Structural Characterization

Structural characterization of the synthesized solids was performed with an X-ray powder diffractometer Shimadzu XRD 6000, using nickel-filtered CuKα (1.54187 Å), operating at 30 kV and 30 mA, 0.02° step size, and 4 s accumulation time. Data was recorded between 2θ = 5-60°. FTIR spectra were obtained using a Bruker VERTEX 70 spectrometer by bulk powder attenuated total reflectance (ATR). The spectra were obtained in the range 400 to 4000 cm^{-1}, with 32 scans, 4 cm^{-1} resolution. Thermal gravimetric analyses (TGA) were performed on a TA Instruments Q500, from

30 to 700°C, at 10°C min^{-1} and dry air flux of 100 mL min^{-1}. The isoelectric point was measured in Malvern Zetasizer Nano – ZS, by dispersing the materials in ultrapure water via sonication. X –ray photoelectron spectroscopy (XPS) analyses were performed on a ScientaOmicron ESCA + spectrometer with a high-performance hemispheric analyzer (EA 125), using a monochromatic Al X-ray excitation source (Kα 1486.7 eV). The samples were supported on carbon adhesive tape.

Morphology was observed by field emission scanning electron microscopy (FEG-SEM, JEOL JSM 6701F microscope). The powder was ultrasonically dispersed and dropped on a silicon plate fixed on the stub. Transmission electron microscopy (TEM) was performed on a TECNAI G2 F10-LaB6 microscope, at 200 kV. Semi-quantitative energy dispersive X-ray analysis (EDX) was performed in the same equipment. The material was prepared as for FEG-SEM, this time using carbon-covered copper grids. BET specific surface area (SSA) was determined by nitrogen adsorption-desorption measurements using a surface area analyzer Micromeritics ASAP–2000.

Diffuse reflectance spectroscopy (DRS) was performed using an Agilent Technologies UV-vis-NIR spectrophotometer model Cary 5G. For estimating the bandgap value from the UV-vis spectrum, a straight line was extrapolated from the Tauc plot [7,24]. Steady-state and time-resolved photoluminescence (SSPL and TRPL) were acquired in a FluoroLog Horiba Jobim Yvon spectrometer, at room temperature, and with excitation at 386 nm acquired with a 300W Xe lamp. For TRPL, emission was evaluated at 517 nm.

3. RESULTS AND DISCUSSION

3.1. g-C_3N_4 Synthesis Optimization and Characterization

The complete g-C_3N_4 optimization steps are detailed in the Supplementary Information [25]. The calculated optimum synthesis conditions (OP) were 605ºC, 183 min, and 5°C min^{-1}, for the annealing temperature, annealing time, and heating rate, respectively. An ANOVA showed that the calculated model was well adjusted to the data, although it could not be considered as a predictive one. Validation experiments were then performed, resulting in a deviation between the estimated and the experimental removals as low as 1.2%, on average. In addition, the removal using the material obtained with the OP conditions was indeed the greatest one, as expected.

The recyclability test showed that the optimized g-C_3N_4 was capable of maintaining its photocatalytic activity at least for seven consecutive batches (Figure S3). It is worthwhile mentioning that those results were achieved without any kind of treatment of the solid, like washing, drying, annealing, etc.

The morphology of g-C_3N_4 samples was analyzed through FEG-SEM in Figure 2a. One can observe that the optimized material was composed of lamellar layers and small particles with indistinct shapes, which are typically aggregates of smaller layered structures (Figure 2b). The main diffraction peak of g-C_3N_4 was observed at 27° (002), corresponding to the stacking of the conjugated aromatic systems [26], indicating that the photocatalyst was properly synthesized (Figure 2c). FTIR spectroscopy indicated the presence of heptazine rings, which have typical bending and stretching vibrations at 810 cm^{-1}, assigned to tri-*s*-triazine, as well as at 1258-1634 cm^{-1}, corresponding to stretching vibrations of aromatic C-N heterocycles [6,27]. The broad band at 2750-3500 cm^{-1} is related to the presence of incomplete or non-perfect segments, corresponding to secondary and primary amines, which are the terminations of the polymeric chain [6,27].

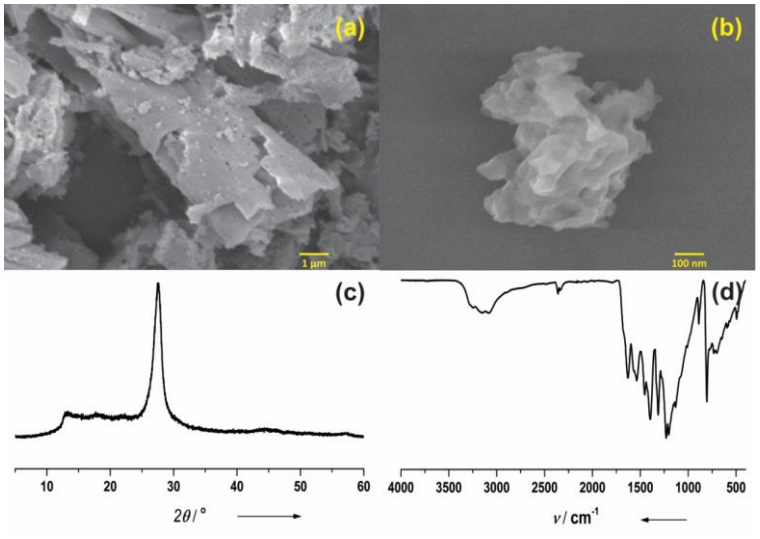

Figure 2. Optimized g-C_3N_4 characterization results: FEG-SEM on different magnifications (a, b); DRX (c) and ATR-FTIR (d).

Table 1 presents the indirect bandgap assessment, which demonstrates that OP and CE samples are active under visible-light irradiation. According to Papailias [6], g-C_3N_4 bandgap energies are directly related to the polymeric chain extension and C-N sp^2 conjugates. It is noteworthy that the OP sample, which had the highest photocatalytic activity, has slightly blue-shifted (on average) than that of CE samples. Although their reduced bandgap energy, CE samples could not achieve high photocatalytic activities, indicating that charge carriers recombined at high rates in those compounds.

Table 1. Bandgap energies, specific surface areas, and isoelectric points of the validation samples.

Sample	Bandgap Energy (eV)	Specific Surface Area ($m^2\ g^{-1}$)	Isoelectric Point
CE1	2.52	14.8	2.8
CE2	2.57	12.9	3.1
CE3	2.51	21.6	3.4
CE4	2.52	25.5	3.2
CE5	2.52	15.1	3.6
OP	2.59	29.5	3.3

In accordance with the previous results, higher SSA has been observed for OP, CE4, and CE3 samples (Table 1), indicating that the elimination of lateral groups gave rise to improved polymeric chains. Higher SSA could improve photocatalytic activity

by making more active sites available. Temperatures and times higher than the ones in the OP conditions decreased the SSA, probably by reducing contribution of the g-C3N4 edges as the polymer chain increases.

The IEP of the OP sample is similar to that of the CE samples (Table 1). In all cases, the IEP ranged between pH 2.8 and 3.6, below typical reported values (pH approximately 4) [9,28]. This indicates that a significant number of basic surface groups have been eliminated from the synthesized materials. Two factors that may influence the IEP, the elimination of surface primary/secondary amines, and the increase in particle sizes (polymer size), reducing the contribution of the edges [28]. Both factors took place in those samples, but apparently the elimination of amines had the largest contribution to the increase of IEP, since particles in all samples had similar sizes.

A remark must be made regarding the comparison of these results with the experimental conditions reported in the literature (Table S6) [29–64] for g-C_3N_4 SSA, bandgap energies, and their related wavelengths. In order to obtain an effective comparison, Table S6 only includes the results for materials without any kind of modifications (e.g. hydro/solvothermal treatment, exfoliation, surface groups' modification, templates, different precursors, special annealing atmosphere, etc.). It is important to mention that those modifications may generate great improvements on SSA and bandgap energies [29-68]; however, their effect could mask the ones caused only by the solid-phase synthesis conditions, which are the parameters optimized in this work.

To better observe the differences among reports, it is proposed a g-C_3N_4 photocatalytic quality factor: the SSA/E_g ratio. Those parameters are related to increased availability of active sites, better formation of the g-C_3N_4 structure, and ease of electron excitation, in this case even under visible light. Therefore, Figure 3 presents that ratio for different reports on the g-C_3N_4 synthesis by the melamine annealing route (with no further modifications).

The optimized synthetic conditions (OP) herein described are more favorable regarding photocatalytic activity, simultaneously presenting greater SSA and lower

bandgap energy, therefore presenting the second-best SSA/E_g ratio. It is noteworthy that, although the material described by Praus [33] presented high SSA and the highest SSA/E_g ratio, it can only be excited under wavelengths on the violet-blue range, which are more energetic than the minimum required by almost all other materials herein assessed.

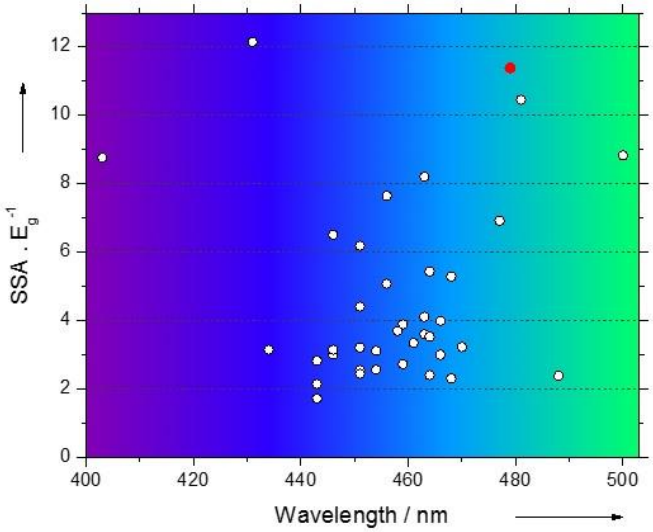

Figure 3. Plot comparing several materials (g-C_3N_4) obtained by solid-phase synthesis only (melamine precursor) reported in the literature (○) and the material herein described (●), regarding their photocatalytic quality factor and absorption wavelength. Survey performed within the Web of Science database using "photocatalysis", "g-C_3N_4", and "melamine" as the search topics. Time span: 2016–2020.

3.2. Sono-assisted g-C_3N_4/WO_3 Heterostructures Formation

Figure 4 depicts a general scheme of ultrasound effect during heterojunction formation. Ultrasound does not directly interact with the oxides precursors; instead, it generates a phenomenon called acoustic cavitation, which could induce physical and chemical changes. Those modifications in the precursor's structures are possible due to the formation, growth, and implosive collapse of bubbles. Following that, short-lived spots are generated where temperature and pressure increase as high as 10,000 K and 1,000 atm, respectively [69]. The selected precursor, H_2WO_4, can generate species that may undergo those changes. In fact, when in contact with H_2O_2, tungstate anions (WO_4^{2-}) form a series of complex ions, whose structures are very sensitive to the experimental conditions [70,71]. WO_4^{2-} ions may also undergo crystallization, in a

process similar to direct annealing of the acid to the formation of WO_3. However, the key mechanisms for this kind of interaction are still unknown.

Simultaneously, the SSA of g-C_3N_4 can be increased (and consequently its photocatalytic activity). The literature reports that bulk g-C_3N_4 layers may be sonochemically exfoliated at acidic medium [72,73]. The g-C_3N_4 protonation causes delamination and increases water dispersibility, but not exfoliation. However, ultrasound does exfoliate g-C_3N_4, increasing SSA tenfold [73]. Oxidation of g-C_3N_4 surface groups and oxygen doping could also play an important role on its final activity, according the literature [48,74]. The herein proposed sono-assisted synthesis rely on reagents that are strong oxidants (peroxide and peroxide-tungsten complexes) and, therefore, oxidation of g-C_3N_4 surface groups may occur.

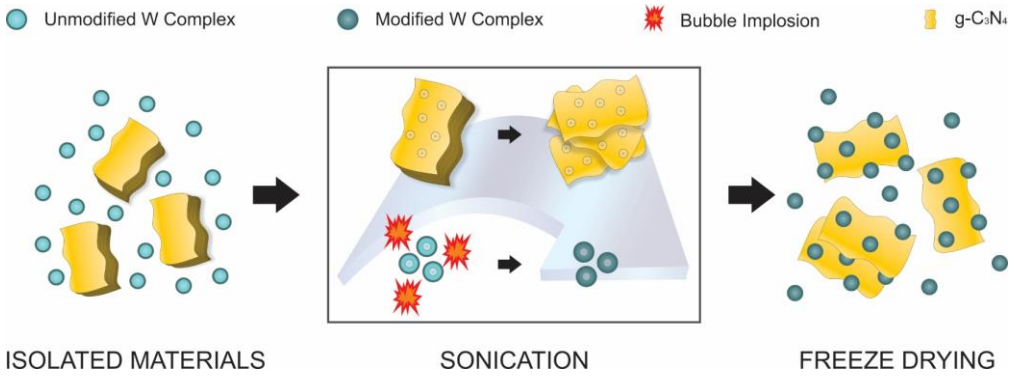

Figure 4. Sequence of modifications on reactional species during the proposed sono-assisted synthetic route.

The sonochemical route can also promote efficient coulombic attractions among reactional species. Specifically, WO_4^{2-} and derived complexes tend to be negatively charged, while g-C_3N_4 is positively charged at acidic media (Table 1). That fact tends to give rise to heterostructures with superior interface formation.

Precursor's mass ratios are described in Table S7. Those values assume that H_2WO_4 would be completely turned into WO_3 by annealing. In fact, TGA demonstrates good accordance between planned and real g-C_3N_4 masses in the heterostructures. TGA also indicates that g-C_3N_4 has relatively high thermal stability, being decomposed only at temperatures higher than 500°C (Figure S8).

3.3. Photocatalytic Activity Evaluation

The photocatalytic activity of the heterostructures during 20 min of irradiation is shown in Figure 5a. One can see that CN60 and CN80 had superior activities than the precursors (CN0 and CN100). Actually, their activity was higher than the sum of the activities of the precursors, suggesting the formation of an effective heterostructure interface. On the other hand, CN20 and CN40 had activities between the ones observed for pure WO_3 and g-C_3N_4. It is noteworthy that the more active samples were the ones with smaller oxidant/g-C_3N_4 molar ratio, suggesting a minimal influence of possible oxidized surface groups. The highest activity was observed with CN80, removing remarkably 95% of the model-pollutant. This result is in accordance with the literature, which reports 70-90% wt. of g-C_3N_4 as the most appropriate content in g-C_3N_4/WO_3 composites for photocatalysis [18,20]. PM sample stands for a physical mixture of the semiconductors, with the same mass ratio of CN80 (most active material). One can notice that the physical mixture could not achieve comparable activity to the analogue heterostructure, suggesting that there was no dissociated-semiconductor assistance and/or synergistic effect.

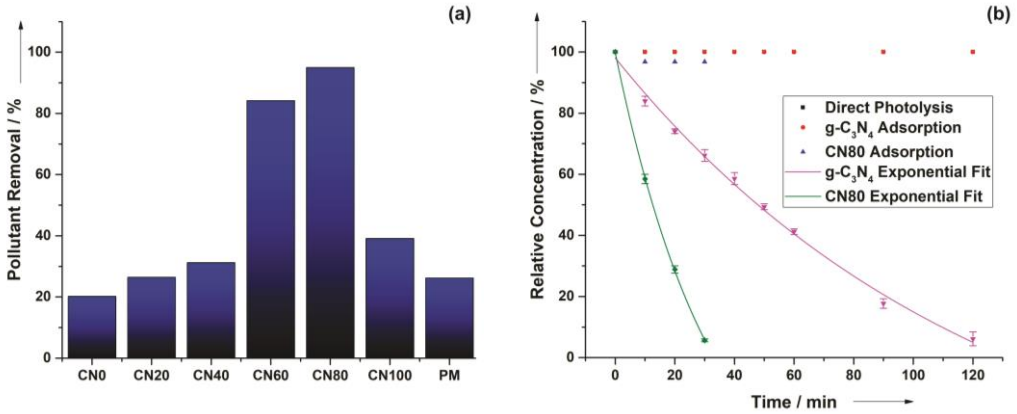

Figure 5. Removal of the model-pollutant (25 mg L^{-1}): (a) after 20 min of photocatalysis with the heterostructures (25 mg each) under UV+Vis irradiation and (b) kinetics by direct photolysis and photocatalysis with g-C_3N_4 and CN80 (also 25 mg each) under visible irradiation.

The degradation kinetics assessment using CN80 and g-C_3N_4 are shown in Figure 5b, as well as direct photolysis. The CN80 heterostructure was selected due to its higher activity (Figure 5a), being compared with the optimized g-C_3N_4. Pure WO_3 only was not evaluated due to its low photocatalytic activity, even under UV+Vis

irradiation. One can see that there was no direct photolysis under Vis irradiation, and that both selected materials could completely remove tartrazine by photocatalysis, although the heterostructure was able to remove the model-pollutant approximately four times faster than optimized g-C_3N_4. The estimated pseudo-first-order kinetic constants were 3.0×10^{-2} and 8.1×10^{-3} min^{-1} for CN80 and g-C_3N_4, respectively. Those results show the high photocatalytic activity improvement obtained in the CN80 heterostructure, both under UV+Vis or Vis irradiation.

3.4. Optical and Structural Characterization

The diffractograms of the heterostructures show a sequential increase in the g-C_3N_4 peaks relative intensity, following their carbon nitride weight percentage and, again, in accordance with the content of the intended composites (Figure 6a). The CN0 diffraction pattern matches the one described in JCBDS 89–4476, for monoclinic WO_3. The major peaks are observed in 23.1, 23.6, and 24.3°, corresponding to the Miller's plans (002), (020), and (200), respectively [10]. According to the literature, this crystalline phase is more appropriate for photocatalytic applications [75,76]. A g-C_3N_4 content as low as in CN20 is enough for distorting the original WO_3 pattern. Higher amounts of carbon nitride lead to a decrease in XRD resolution, which was probably caused by the interference of the relatively low g-C_3N_4 crystallinity.

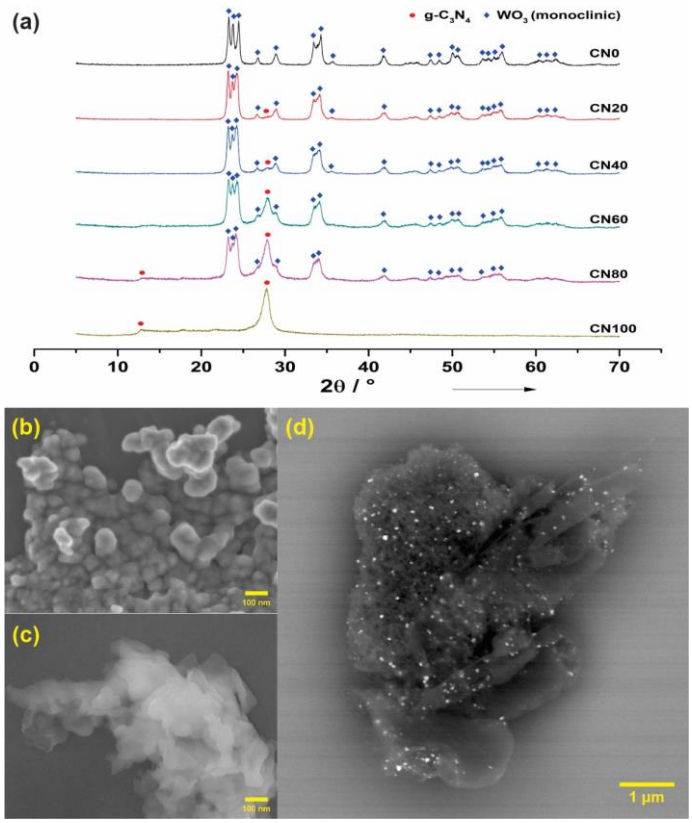

Figure 6. Characterizations of CN samples: (a) DRX; FEG-SEM microscopies of (b) CN0 and (c) CN100; and backscattering electron microscopy of (d) CN80.

FEG-SEM presents very distinct morphologies for CN0 and CN100 (Figure 5b-c). Pure graphitic carbon nitride seems to be formed by an agglomerate of lamellar structures, even after a possible exfoliation step by ultrasound irradiation. On the other hand, tungsten trioxide is formed by irregular particles, with no characteristic shape. However, it was difficult to distinguish those differences in the heterostructures. This difficulty could be explained by the similar particle sizes of WO_3 and g-C_3N_4, and/or high dispersions of WO_3 on g-C_3N_4. Therefore, backscattering electron microscopy was performed, with the same conditions, to check the latter hypothesis. As one can observe in Figure 6d, smaller and brighter spots representing WO_3 were well distributed over darker spots (g-C_3N_4). Similar images for the other heterostructures are shown in the Supplementary Information (Figure S9). The same behavior was observed with the EDX analysis (Figure 6), which shows that carbon (yellow), nitrogen (purple), oxygen (green), and tungsten (cyan) are indeed homogenously distributed.

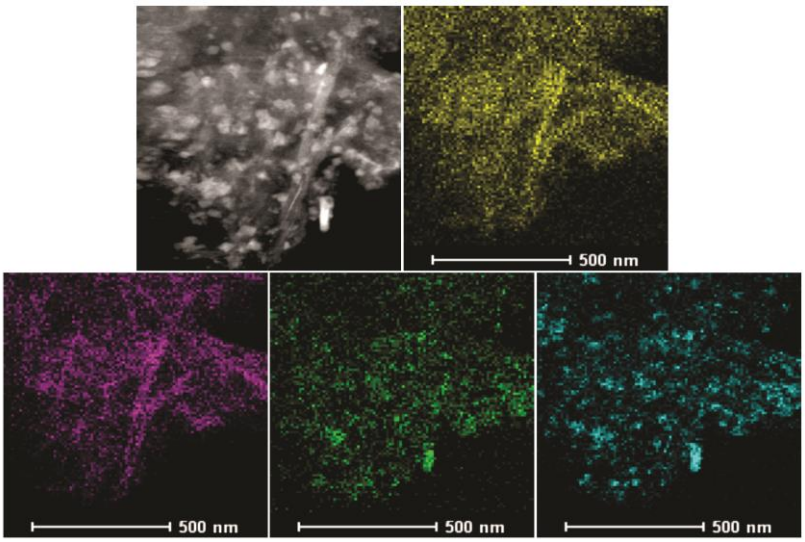

Figure 7. Distribution of elements according to the EDX analysis: carbon (yellow), nitrogen (purple), oxygen (green), and tungsten (cyan).

High-resolution TEM could not directly highlight the diffraction planes of pure g-C_3N_4. However, WO_3 presents a sequence of parallel lines with 0.27-nm gaps, representing its (022) Miller's plane (Figure 8a). The absence and presence of diffraction planes in g-C_3N_4 and WO_3, respectively, made it possible to observe regions mostly composed of these substances, as well as their interface. Figure 8b shows this behavior, presenting visible diffraction peaks (0.38-nm gaps, 020 plane) at top-left and the absence of them at bottom-right. Between those regions, an interface can be noticed, presenting barely visible planes. This image highly suggests the formation of g-C_3N_4/WO_3 heterojunctions, and consequently, charge carriers transference between the two materials.

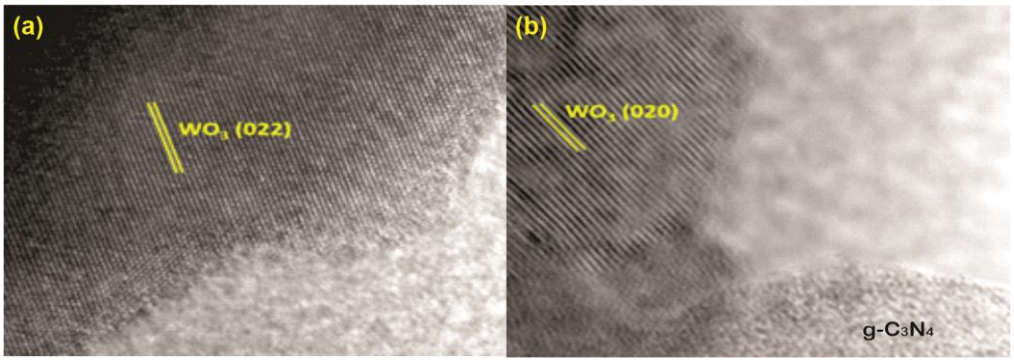

Figure 8. High-resolution TEM of (a) CN0 and (b) CN80.

Figures 9a-9c compare the XPS spectra of g-C_3N_4 (OP) and CN80; Figure 9d compares WO_3 and CN80 spectra. XPS survey spectra are presented in Figure S10. The C 1s spectra (Figure 9a) show a clear peak on 284.8 eV for adventitious carbon, which was used for calibration of further peaks [77]. Although not shown in Figure 9a, the WO_3 sample also had its peaks calibration based on adventitious carbon. Both g-C_3N_4 and CN80 presented a peak at 288.1 eV, that could be related to N=C–N tertiary carbon [78-80]. Peaks at 286.0 and 287.6 eV were associated to C–O and C=O, respectively. Those peaks could be caused by the samples contamination (adventitious carbon) [78,81]. Peaks around 286.0 eV could also be related to C–N bonds. Figure 9b presents g-C_3N_4 peaks at 398.2, 399.5, and 403.1, assigned to C=N–C sp^2 nitrogen, tertiary N–$(C)_3$ nitrogen, and π-excitation of nitrogen, respectively [78, 82-84]. For CN80, nitrogen binding energies followed the same pattern, but were shifted approximately +0.4 eV, probably due to positive charging effects [77]. The O 1s spectrum (Figure 9c) shows peaks at 531.3 and 533.1 eV for both g-C_3N_4 and CN80, assigned to superficial hydroxyl groups and adsorbed water, respectively [78,84,85]. The presence of those peaks on g-C_3N_4 suggests that its surface was already somewhat oxidized, however the slightly increase at the 531.3 eV peak of CN80 could suggest that there was a minimal oxidation of surface groups during its synthesis. CN80 also presents a peak at 530.4 eV, related to the O–W binding energy [86]. Tungsten-related binding energies of WO_3 were: 35.5, 37.6, and 41.1 eV ($W4d_{7/2}$, $W4d_{5/2}$, and loss feature, respectively) [87]. The shift to low biding energies observed in CN80 suggested that part of the tungsten changed its oxidation state, from +6 to +5. That fact is possible due to the stability of tungsten oxide polymorphs, which can be formed in the surface by oxygen disbalancing. However, as the XRD pattern of WO_3 did not change (in comparison with pristine WO_3), one can conclude that this effect is limited, probably at the surface. Similar assessment regarding fresh and used CN80 can be observed in Figure S11. Generally, the patterns of the peaks did not change significantly after photocatalysis. However, their relative intensities suggested that there was a simultaneous decrease of hydroxyl surface groups, sp^2 nitrogen, and tungsten with $W4d_{7/2}$ states. These factors may be associated to tungsten and g-C_3N_4 terminal C-N oxidation, although in a minor extent.

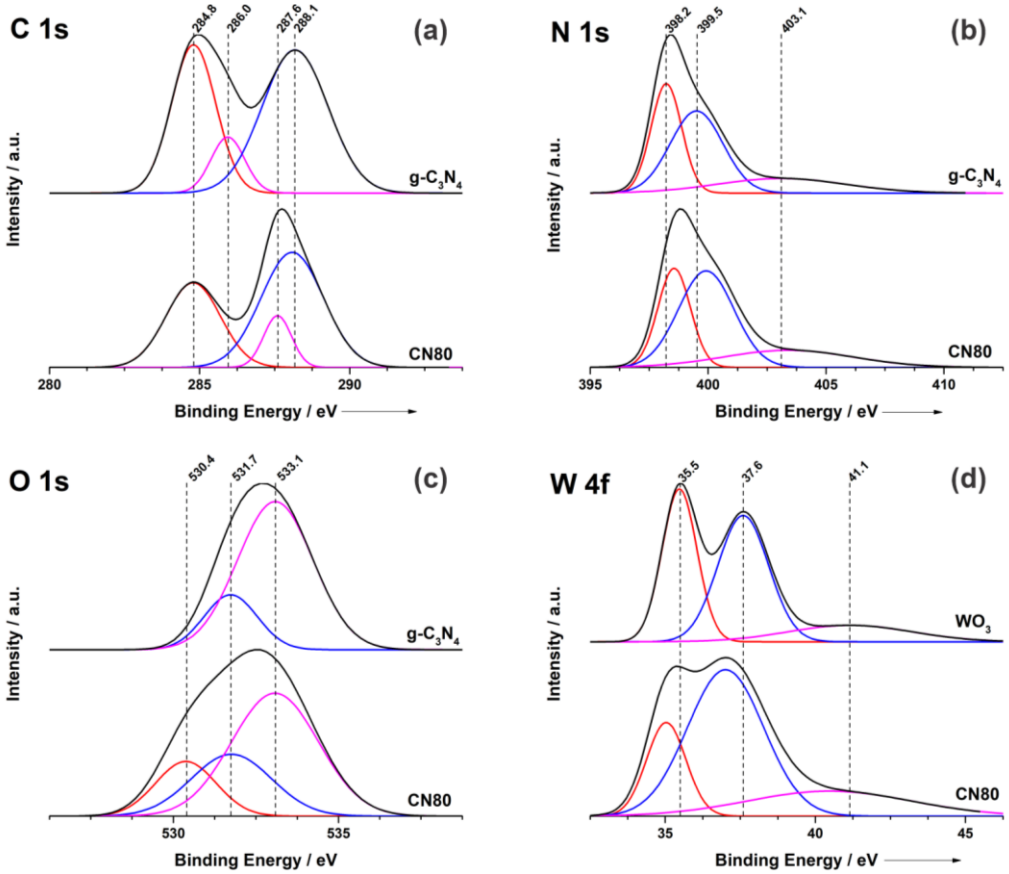

Figure 9. High resolution XPS spectra of g-C_3N_4 (OP), WO_3, and CN80: (a) C 1s, (b) N 1s, (c) O 1s, and (d) W 4f.

Table 2 shows the measured SSA for the synthesized heterostructures. One can observe that precursors areas were in the same order of magnitude: 20.0 and 29.7 $m^2 g^{-1}$ for WO_3 and g-C_3N_4, respectively. Composites presented increasing SSA, related to their g-C_3N_4 content. As optimized (OP) and sonicated (CN100) g-C_3N_4 presented similar SSA, one suggests that ultrasound irradiation was not energetic enough to achieve exfoliation or the obtained exfoliation was lost at some point of the synthetic route. Perhaps the quick solidification of the suspension in the freeze-drying step promoted the re-agglomeration of previously exfoliated sheets. Even if that is the case, g-C_3N_4 exfoliation was important for allowing WO_3 particles be intercalated between g-C_3N_4 layers, increasing their contact area.

Table 2 also presents the indirect bandgap estimation, which demonstrates that precursors have similar bandgap energies, as well as the heterostructures with high g-C_3N_4 contents. Although CN20 and CN40 had slightly lower bandgaps (compared to the precursors), they did not present higher photocatalytic activities (Figure 5). These results may indicate that charge carriers readily recombined in those compounds. In any

case, the differences among samples suggest that different energy configurations were formed, significantly changing light absorption.

Table 2. Specific surface area (m^2 g^{-1}) and bandgap energies (eV) of heterostructure samples.

Sample	Specific surface area (m^2 g^{-1})	Bandgap energy E_g (eV)
CN0	20.0	2.54
CN20	22.3	2.45
CN40	24.1	2.44
CN60	28.6	2.62
CN80	28.6	2.53
CN100	29.7	2.57

Finally, regardless of the heterostructures composition, the characterization performed indicated that they had similar properties. In fact, none of the samples presented any difference that could justify the higher photocatalytic activity observed. Therefore, removal increases could only be ascribed to electronical properties induced by an effective interface between the two precursors. The following experiments were performed aiming at proving that hypothesis.

3.4. Band Structure and Photocatalysis Mechanisms Proposition

To better understand the photo-generated charge carriers separation in the heterostructures, conduction (CB) and valence (VB) bands energy positions were estimated. According to Mousavi [88], the theoretical energy levels of the bands can be calculated by Equations 1 and 2. E_{CB} and E_{VB} are the CB and VB energy potentials, respectively; E^e is the energy of the free electron versus the normal hydrogen electrode (NHE), approximately 4.5 eV; χ represents the Mulliken's electronegativity of semiconductors. According to the literature [89,90] , they are 4.73 and 6.59 eV for g-C_3N_4 and WO_3, respectively.

$$E_{CB} = \chi - E^e - 0.5E_g \quad (1)$$

$$E_{VB} = E_{CB} + E_g \quad (2)$$

Therefore, the calculated E_{CB} and E_{VB} for g-C_3N_4 (OP sample) were – 1.06 and + 1.52 eV, respectively. Those figures for WO_3 were + 0.82 and + 3.36 eV, respectively. It was assumed that the E_{CB} and E_{VB} of each precursor in the synthesized heterostructures were the same. In order to empirically assess VB values for those samples, an extrapolation of the slope of their first XPS signal was performed (Figure 10) [91]. One can notice that the empirical values were in agreement with the theoretical ones (+1.47 eV and +3.14 eV for g-C_3N_4 and WO_3, respectively). The slightly differences between theoretical and empirical values could be explained by the Mullikan electronegativity: tabled values may not exactly represent the real ones.

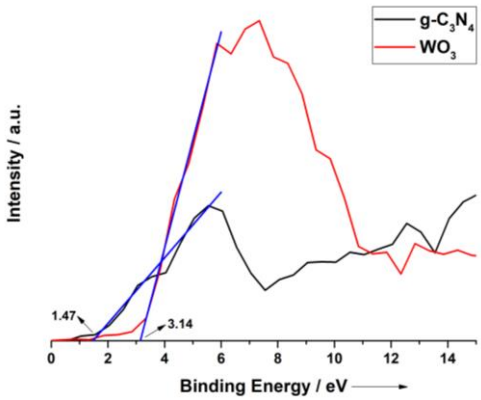

Figure 10. Valence band assessment via X-ray photoelectron spectroscopy extrapolation.

It is well known that radicals (hydroxyl and superoxide) and holes are the predominant oxidant species in photocatalysis [92]. Therefore, it is of utmost importance to realize whether the materials E_{CB} and E_{VB} are correctly positioned to generate those species, making it possible the proposition of the involved mechanism.

One can observe that g-C_3N_4 (OP sample) is able to reduce adsorbed O_2 to $^{\bullet}O_2^-$, as its CB is more negative than the standard potential of $O_2/^{\bullet}O_2^-$ (– 0.13 eV) [93]. On the contrary, WO_3 cannot generate superoxide radical by that route. g-C_3N_4 holes cannot oxidize OH^- or H_2O to form hydroxyl radicals, once they are less positive than + 1.89 and + 2.72 eV, which are the standard potentials of $OH^-/OH^{\bullet}$ and $H_2O/OH^{\bullet}$, respectively [94]. However, both reactions can take place at WO_3 holes. A third (indirect) route to form hydroxyl radicals is the reduction of O_2 to H_2O_2 in the presence of H_3O^+ [93]. Both semiconductors can promote that reaction (+ 0.68 eV).

To empirically observe the effects of those assumptions, scavengers (20 mmol L^{-1}) were added to a typical photocatalytic reaction with the CN80 heterostructure: propan-2-ol (IPA), potassium iodide (KI), and benzoquin-1,4-one (BQ) were used as scavengers of hydroxyl radicals, holes, and superoxide radicals, respectively [95]. Figure 11 presents the pollutant removal achieved with and without those scavengers.

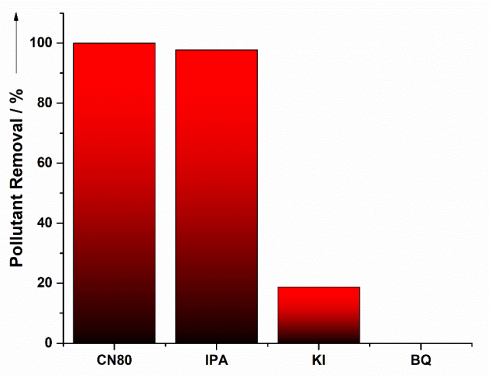

Figure 11. Model-pollutant removal by the CN80 heterostructure with and without scavengers: propan-2-ol (IPA), benzoquin-1,4-one (BQ), and potassium iodide (KI).

The results showed that $^{\bullet}OH$ is not significantly involved in the degradation of tartrazine, as the addition of IPA caused a slight reduction in its removal, probably within the experimental error. On the contrary, BQ totally prevented the pollutant removal, which implies the paramount role of $^{\bullet}O_2^-$ radical. These facts indicate that a significant amount of electrons was transferred to the CB of g-C_3N_4 upon excitation, which is the only one capable of $^{\bullet}O_2^-$ formation. The classic type-II scheme for the synthesized heterostructure does not hold, as electrons should be more stable in the CB of WO_3 in this kind of configuration.

The addition of KI decreased removal quite significantly (approximately 80%), showing that holes also had great importance for the degradation process. As $^{\bullet}OH$ did not have any perceivable role (IPA addition), probably the direct oxidation of tartrazine took place at the VB of WO_3, the only band positive enough to promote that.

PL analysis (electron excitation intensity and excited electron lifetime) also helps in deducting the degradation mechanism. Figure 12a shows an increase in the SSPL intensity of the g-C_3N_4/WO_3 heterostructure (CN80) compared to that of optimized g-C_3N_4. At first sight, this result would indicate that CN80 has higher charge

carriers recombination rate and, consequently, lower photocatalytic activity. However, that hypothesis is not corroborated by the degradations achieved. Therefore, another path for the electrons was indicated.

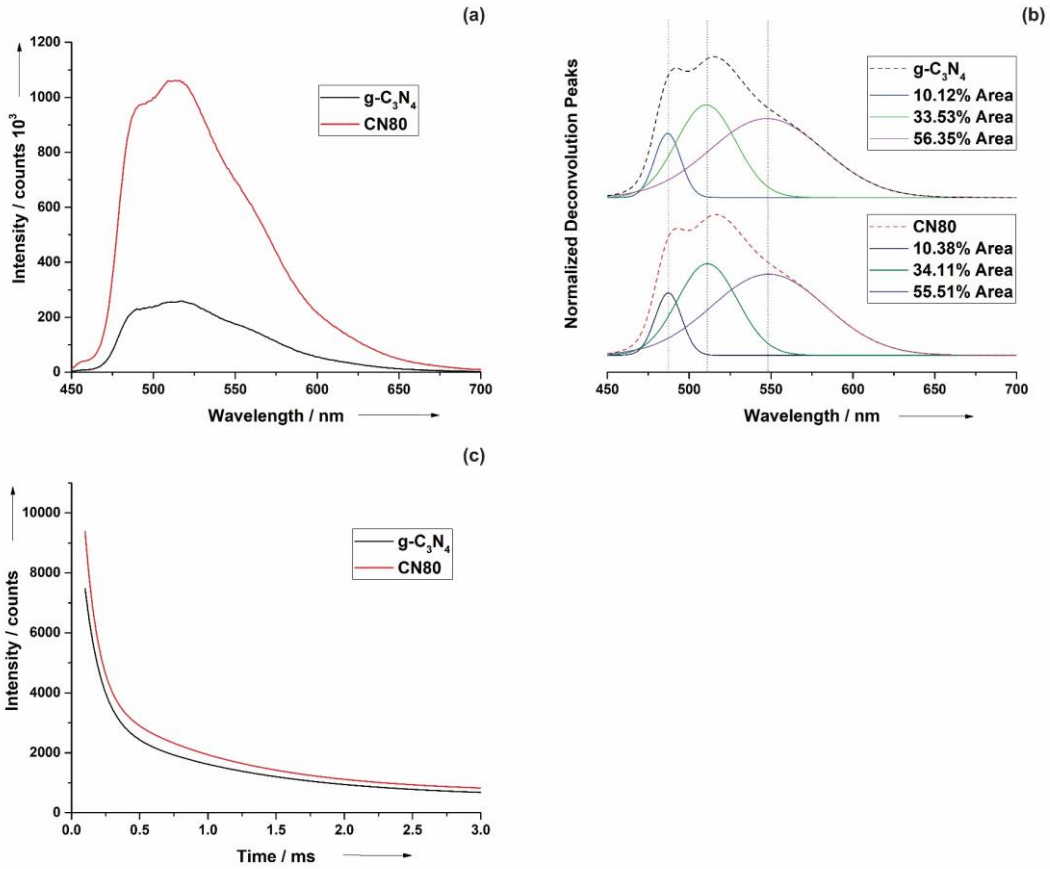

Figure 12. (a) SSPL. (b) Normalized deconvolution of SSPL spectra for g-C_3N_4 and CN80. Percentages are related to the total area of the reconstructed SSPL (dashed). (c) TRPL for g-C_3N_4 and CN80.

According to the literature, the excited electrons in typical type-II heterostructures can be transferred between conduction bands and, therefore reducing PL intensity, as electrons may return to the fundamental state by different routes [96]. In fact, that could lead to band shifts on the heterostructure emission spectrum. However, the results indicated that there were no new PL phenomena on heterostructure, as could be seen in Figure 12b.

Figure 12b presents the normalized deconvolution peaks for g-C_3N_4 and CN80, as well as the reconstructed SSPLs (sum of deconvoluted peaks, dashed) and the relative area of each peak. One can notice that the peaks maxima are aligned and the relative areas deviation was not larger than 1% between g-C_3N_4 and CN80. Those facts

suggest that the same PL phenomena is taking place in both materials, although with different intensities. In other words, although WO_3 electrons could be excited by the light source, only the standard decay of g-C_3N_4 emission has been observed.

Therefore, based on the difference between the CB of WO_3 and g-C_3N_4, the scavenger effect, and the absence of SSPL band shifts, it is proposed that the transfer of excited electrons between those bands is neglectful. Alternatively, theoretical and empirical experiments suggest the formation of Z-scheme heterojunctions, in which excited electrons might flow from the VB of WO_3 to the CB of g-C_3N_4 [41,97]. That multi-step process comprises: the excitation of electrons from the VB of WO_3 to its CB; their transfer to the VB of g-C_3N_4, and finally the excitation of those electrons to the CB of g-C_3N_4.

If the interface of that Z-scheme heterojunction is highly effective, all of the WO_3 excited electrons might flow to g-C_3N_4. That electrons excess in the VB of g-C_3N_4 could be the reason for the increase observed in the heterostructure SSPL, with massive excitation to the CB and relaxation to the respective fundamental state. That would explain the significant formation of superoxide radicals from the reduction of adsorbed oxygen.

Figure 10c shows the TRPL results, which were adjusted to a bi-exponential function (Equation 3), in which I is PL intensity (counts) and t is time (μs). Direct band-to-band radiative (1) and inter-sheet (2) recombination processes are represented by A_1, A_2 and τ_1, τ_2, which are the relative contributions and the lifetimes of each process, respectively. The calculated averaged lifetimes for g-C_3N_4 and CN80 were 0.82 and 0.89 μs, which demonstrates an improvement on the charge carriers availability for surface redox reactions in the heterostructure. Those calculations were performed according to Alam [98].

$$I(t) = A_1 e^{-t/\tau_1} + A_2 e^{-t/\tau_2} \quad (3)$$

Finally, this set of experiments corroborates the formation of an efficient interface and, consequently, heterojunction between the two photocatalysts. Moreover, the results of the experimental and theoretical band positions assessment, photocatalytic activity in the presence of inhibitors, and steady-state photoluminescence suggest the formation of a

Z-scheme heterostructures (Figure 13) [97,99,100]. That charge-transfer pathway imply high charge carrier separation, in accordance with the time-resolved photoluminescence results.

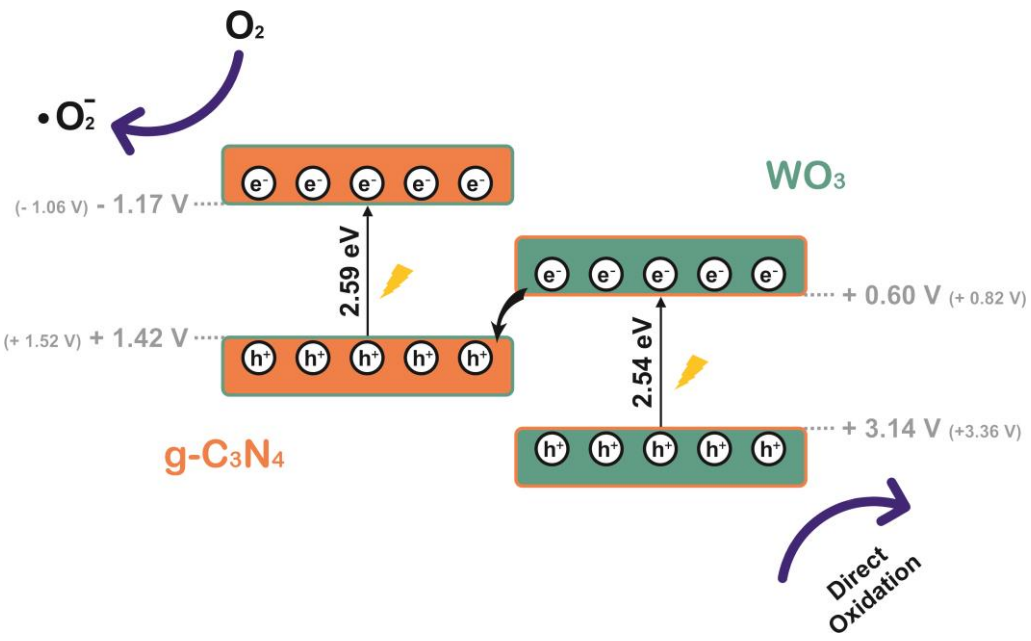

Figure 13. Proposed photocatalysis mechanism for g-C_3N_4/WO_3 heterostructures. Theoretical CBs and VBs positions inside brackets.

4. CONCLUSIONS

- This paper shows the importance of performing optimization routines to assess the true efficiency of any system or material of interest. By carefully optimizing the g-C_3N_4 solid-phase synthesis, it was possible to fabricate a material with superior photocatalytic activity, at least as far as bandgap energies and specific surface areas are concerned.

- The sono-assisted synthesis of the g-C_3N_4/WO_3 composite, using tungsten peroxo-complexes with the direct incorporation of g-C_3N_4 followed by freeze-drying was proven to be a facile procedure, able to produce effective heterojunctions.

- The synthesized g-C_3N_4/WO_3 composite presented high photocatalytic activity under visible light, being capable of completely degrading the model-pollutant in a short time by pseudo-first-order kinetics.

- Based on the measured bandgaps, valence and conduction bands energy levels, the results indicated that superoxide radicals and holes were the active species during degradation. That finding was corroborated by performing tests with scavengers.

- The calculated energy levels for valence and conduction bands together with scavengers tests and steady-state photoluminescence results, indicated the formation of a Z-scheme heterostructure.

ACKNOWLEDGEMENTS

The authors would like to thank The National Council for Scientific and Technological Development (CNPq), The Coordination for the Improvement of Higher Education Personnel (CAPES – Finance Code 001), São Paulo Research Foundation (FAPESP), processes # 2014/02739–6, 2015/14330–8, and 2018/01258-5 and The Research Network of Nanotechnology Applied to Agribusiness (AgroNano Network/Embrapa, MCTI-SisNano) for financial support.

REFERENCES

[1] P. Mukherjee, P. Ray, Major challenges in the design of a large-scale photocatalytic reactor for water treatment, Chem. Eng. Technol. 22 (1999) 253-260. https://doi.org/10.1002/(SICI)1521-4125(199903)22:3<253::AID-CEAT253>3.0.CO;2-X

[2] S. Cao, J. Low, J. Yu, M. Jaroniec, Polymeric photocatalysts based on graphitic carbon nitride, Adv. Mat. 27 (2015) 2150-2176. https://doi.org/10.1002/adma.201500033

[3] S. Ye, R.Wang, M. Wu, Y. Yuan, A review on g-C_3N_4 for photocatalytic water splitting and CO_2 reduction, App. Surf. Sci. 358 (2015) 15-27. https://doi.org/10.1016/j.apsusc.2015.08.173

[4] B. Jürgens, E. Irran, J. Senker, P. Kroll, H. Müller, W. Scnick, Melem (2,5,8-triamino-tri-s-triazine), an important intermediate during condensation of melamine rings to graphitic carbon nitride: synthesis, structure determination by X-ray powder diffractometry, solid-state NMR, and theoretical studies, J. Am. Chem. Soc. 125 (2003) 10288-10300. https://doi.org/10.1021/ja0357689

[5] I. Papailias, N. Torodova, T. Giannakopoulou, S. Karapati, N. Boukos, D. Dimotikali, C. Trapalis, Enhanced NO_2 abatement by alkaline-earth modified g-C_3N_4 nanocomposites for efficient air purification, App. Surf. Sci. 430 (2018) 225-233. https://doi.org/10.1016/j.apsusc.2017.08.084

[6] I. Papailias, T. Giannakopoulou, T. Todorova, D. Demotiakli, T. Vaimakis, C. Trapalis, Effect of processing temperature on structure and photocatalytic properties of g-C_3N_4. App. Surf. Sci. 358 (2015) 278-286. https://doi.org/10.1016/j.apsusc.2015.08.097

[7] J. Zhang, Y. Chen, X. Wang, Two-dimensional covalent carbon nitride nanosheets: synthesis, functionalization, and applications, Energy Environ. Sci. 8 (2015) 3092-3108. https://doi.org/10.1039/C5EE01895A

[8] C. Janáky, K. Rajeshwar, N. Tacconi, W. Chanmanee, M. Huda, Tungsten-based oxide semiconductors for solar hydrogen generation, Catal. Today 199 (2013) 53–64. https://doi.org/10.1016/j.cattod.2012.07.020

[9] Z. Huang, J. Song, L. Pan, X. Zhang, L. Wang, J. Zou, Tungsten oxides for photocatalysis, electrochemistry, and phototherapy, Adv. Mat. 27 (2015) 5309–5327. https://doi.org/10.1002/adma.201501217

[10] W. Kwong, N. Savvides, C. Sorrell, Electrodeposited nanostructured WO_3 thin films for photoelectrochemical applications, Electrochim. Acta 75 (2012) 371–380. https://doi.org/10.1016/j.electacta.2012.05.019

[11] C. Granqvist, Electrochromic tungsten oxide: review of progress 1993-1998. Sol. Energy Mater. Sol. Cells 60 (2000) 201–262. https://doi.org/10.1016/S0927-0248(99)00088-4

[12] I. Georgaki, D. Kenanakis, N. Katsarakis, Synthesis of WO_3 catalytic powders : evaluation of photocatalytic activity under NUV/visible light irradiation and alkaline reaction pH, J. Sol-Gel Sci. Techn. (2015) 120–128. https://doi.org/10.1007/s10971-015-3758-5

[13] S. Zhuiykov, E. Kats, K. Kalantar-Zadeh, Enhanced electrical properties in sub-10-nm WO_3 nanoflakes prepared via a two-step sol-gel-exfoliation method, Nanoscale Res. Lett. 9 (2014) 401–410. https://doi.org/10.1186/1556-276X-9-401

[14] J. Yu, L. Qi, Template-free fabrication of hierarchically flower-like tungsten trioxide assemblies with enhanced visible-light-driven photocatalytic activity, J. Hazard. Mater. 169 (2009) 221–227. https://doi.org/10.1016/j.jhazmat.2009.03.082

[15] S. Adhikari, D. Sarkar, Hydrothermal synthesis and electrochromism of WO_3 nanocuboids. RSC Adv. 4 (2014) 20145-20153. https://doi.org/10.1039/C4RA00023D

[16] Z. Wang, M. Hu, Y. Qin, Solvothermal synthesis of WO_3 nanocrystals with nanosheet and nanorod morphologies and the gas-sensing properties, Mater. Lett. 171 (2016) 146-149. https://doi.org/10.1016/j.matlet.2016.02.040

[17] A. Navarro-Aguilar, S. Obregón, D. Sanchez-Martinez, D. Henández-Uresti, An efficient ans stable WO_3/g-C_3N_4 photocatalyst for ciprofloxacin and orange G degradation, J. Photochem. Photobiol. A 384 (2019) 112010-112016. https://doi.org/10.1016/j.jphotochem.2019.112010

[18] I. Aslam, The synergistic effect between WO_3 and g-C_3N_4 towards efficient visible-light-driven photocatalytic performance, New J. Chem. 38 (2014) 5462–5469. https://doi.org/10.1039/C4NJ01370K

[19] J. Ding, Q. Liu, Z. Zhang, X. Liu, J. Zhao, S. Cheng, B. Zong, W. Dai, Carbon nitride nanosheets decorated with WO_3 nanorods: ultrasonic-assisted facile synthesis and catalytic application in the green manufacture of dialdehydes. Appl. Catal. B 165 (2015) 511-518. https://doi.org/10.1016/j.apcatb.2014.10.037

[20] K. Katsumata, R. Motoyoshi, N. Matsushita, K. Okada, Preparation of graphitic carbon nitride g-C_3N_4/WO_3 composites and enhanced visible-light-driven photo-degradation of acetaldehyde gas, J. Hazard. Mater. 260 (2013) 475–482. https://doi.org/10.1016/j.jhazmat.2013.05.058

[21] M.A. Bezerra, R.E. Santeli, E.P. Oliveira, L.S. Villar, L.A. Escaleira, Response surface methodology (RMS) as a tool for optimization in analytical chemistry. Talanta 76 (2008) 965-977. https://doi.org/10.1016/j.talanta.2008.05.019

[22] A. Hernández-Ramírez, I. Medina-Ramírez, Photocatalytic Semiconductors: Synthesis, Characterization, and Environmental Applications, Springer, New York, 2015.

[23] S. Karakus, Sonochemical Reactions, IntechOpen, Istambul, 2020.

[24] J. Tauc, R. Grigorovici, R. Vancu, Optical properties and electronic structure of amorphous germanium, Phys. Status Solidi 15 (1966) 627-637. https://doi.org/10.1002/pssb.19660150224

[25] R.E. Bruns, I.S. Scarminio, B. Neto ,Statistical Design – Chemometrics, Elsevier Science, Amsterdam, 2006.

[26] L. Shi, L. Liang, F. Wang, J. Ma, J. Sun, Polycondensation of guanidine hydrochloride into a graphitic carbon nitride semiconductor with a large surface area as a visible light photocatalyst, Catal. Sci. Technol. 4 (2014) 3235-3243. https://doi.org/10.1039/C4CY00411F

[27] P. Wu, J. Wang, J. Xhang, L. Guo, F. Osterloh, Structure defects in g-C_3N_4 limit visible light driven hydrogen evolution and photovoltage, J. Mater. Chem. A 2 (2014) 20338-20344. https://doi.org/10.1039/C4TA04100C

[28] B. Zhu, P. Xia, W. Ho, J. Yu, Isoelectric point and adsorption activity of porous g-C_3N_4, Appl. Surf. Sci. 344 (2015) 188-195. https://doi.org/10.1016/j.apsusc.2015.03.086

[29] L. Wang, Y. Hong, E. Liu, Z. Wang, J. Chen, S. Yang, J. Wang, X. Lin, J. Shi, Rapid polymerization synthesizing high-crystalline g-C_3N_4 towards boosting solar photocatalytic H_2 generation, Int. J. Hydrogen Energy 2020. https://doi.org/10.1016/j.ijhydene.2019.12.168

[30] D. Han, J. Liu, H. Cai, L. Kong, J. Wang, H. Shi, Q. Guo, X. Fan, High-yield and low-cost method to synthesize large-area porous g-C_3N_4 nanosheets with improved photocatalytic activity for gaseous nitric oxide and 2-propanol photodegradation, Appl. Surf. Sci. 464 (2019) 577-585. https://doi.org/10.1016/j.apsusc.2018.09.108

[31] X. Li, X. Qian, X. An, J. Huang, Preparation of a novel composite comprising biochar skeleton and “chrysanthemum” g-C_3N_4 for enhanced visible light photocatalytic degradation of formaldehyde, Appl. Surf. Sci. 487 (2019) 1262-1270. https://doi.org/10.1016/j.apsusc.2019.05.195

[32] V. Matějka, M. Sihor, M. Reli, A. Martaus, K. Kočí, M. Kormunda, P. Praus, Composites g-C_3N_4 and $BiOIO_3$ for photocatalytic decomposition of N_2O, Mater. Sci. Semicond. Process. 100 (2019) 113-122. https://doi.org/10.1016/j.mssp.2019.04.036

[33] P. Praus, J. Lang, A. Martaus, L. Svoboda, V. Matejka, M. Kormunda, M. Sihor, M. Reli, K. Kočí, Composites of $BiVO_4$ and g-C_3N_4: Synthesis, Properties and Photocatalytic Decomposition of Azo Dye AO7 and Nitrous Oxide, J. Inorg. Organomet. Polym. Mater. 29 (2019) 1219-1234.

[34] A. Raza, H. Shen, A. Haidry, S. Cui, Hydrothermal synthesis of Fe_3O_4/TiO_2/g-C_3N_4: Advanced photocatalytic application, Appl. Surf. Sci. 488 2019 887-895. https://doi.org/10.1016/j.apsusc.2019.05.210

[35] M. Reli, I. Troppová, M. Sihor, J. Pavlovský, P. Praus, K. Kočí, Photocatalytic decomposition of N_2O over g-C_3N_4/$BiVO_4$ composite, Appl. Surf. Sci. 469 (2018) 181-191. https://doi.org/10.1016/j.apsusc.2018.10.255

[36] Y. Xu, L. Zhang, J. Chen, Y. Fu, Q. Li, J. Yin, Z. Cheng, W. Kan, P. Zhao, H. Zhong, Y. Zhao, X. Wang, Synthesis of nano-Ag-assisted attapulgite/g-C_3N_4 composites with superior visible light photocatalytic performance, Materials Chemistry and Physics, 221 (2019) 447-456. https://doi.org/10.1016/j.matchemphys.2018.09.065

[37] H. Yan, Z. Zhu, Y. Long, W. Li, Single-source-precursor-assisted synthesis of porous WO_3/g-C_3N_4 with enhanced photocatalytic property, Colloids Surf. A 582 (2019) 123857. https://doi.org/10.1016/j.colsurfa.2019.123857

[38] J. Zhang, J. Mei, S. Yi, X. Guan, Constructing of Z-scheme 3D g-C_3N_4-ZnO@graphene aerogel heterojunctions for high-efficient adsorption and photodegradation of organic pollutants, Appl. Surf. Sci., 492 (2019) 808-817. https://doi.org/10.1016/j.apsusc.2019.06.261

[39] E. Azimi, A. Badiei, M. Sadr, Dramatic visible photocatalytic performance og g-C_3N_4-based nanocomposite due to the synergistic effect of AgBr and ZnO semiconductors, J. Phys. Chem. Solids 122 (2018) 174-183.

[40] M. Bellardita, E.E. Garcia-Lopez, G. Marci, I. Krivtsov, J.R. Gracia, L. Palmisano, Selective photocatalytic oxidation of aromatic alcohols in water by using P-doped g-C_3N_4, Appl. Catal. B 220 (2018) 222-233. https://doi.org/10.1016/j.apcatb.2017.08.033

[41] L. Jiang, Z. Yuan, G. Zeng, J. Liang, X. Chen, H.Yu, H. Wang, Z. Wu, J. Zhang, T. Xiong, In-situ synthesis of direct solid-state dual Z-scheme WO_3/g-C_3N_4/Bi_2O_3 photocatalyst for the degradation of refractory pollutant, Appl. Catal. B 227 (2018) 376-385. https://doi.org/10.1016/j.apcatb.2018.01.042

[42] C. Liu, H. Huang, W. Cui, F. Dong, Y. Zhang, Band structure engineering and efficient charge transport in oxygen substituted g-C_3N_4 for superior photocatalytic hydrogen evolution, Appl. Catal. B 230 (2018) 115-124. https://doi.org/10.1016/j.apcatb.2018.02.038

[43] Y. Mao, M. Wu, G. Li, P. Dai, X. Yu, Z. Bai, P. Chen, Photocatalytic degradation of methylene blue over boron-doped g-C_3N_4 together with nitrogen-vacancies under visible light irradiation, React. Kinet. Mech. Cat. 125 (2018) 1179-1190. https://doi.org/10.1007/s11144-018-1414-0

[45] P. Praus, L. Svoboda, R. Dvorsky, M. Reli, Nanocomposites of SnO_2 and g-C_3N_4: Preparation, characterization and photocatalysis under visible LED irradiation, Ceram. Int. 44 (2018) 3837-3846. https://doi.org/10.1016/j.ceramint.2017.11.170

[46] Z. Shu, C. Xie, J. Zhou, T. Li, Y. Chen, W. Wang, Z. Zhao, Nanoporous g-C_3N_4 nanosheets: Facile synthesis and excellent visible-light photocatalytic H_2 evolution performance, J. Alloys Compd. 747 (2018) 140-148. https://doi.org/10.1016/j.jallcom.2018.03.019

[47] Y. Tan, Z. Shu, J. Zhou, T. Li, W. Wang, Z. Zhao, One-step synthesis of nanostructured g-C_3N_4/TiO_2 composite for highly enhanced visible-light photocatalytic H_2 evolution, Appl. Catal. B 230 (2018) 260-268. https://doi.org/10.1016/j.apcatb.2018.02.056

[48] Y. Zeng, X. Liu, C. Liu, L. Wang, X. Xia, S. Zhang, S. Luo, Y. Pei, Scalable one-step production of porous oxygen-doped g-C_3N_4 nanorods with effective electron separation for

excellent visible-light photocatalytic activity, Appl. Catal. B (2018) 224 1-9. https://doi.org/10.1016/j.apcatb.2017.10.042

[49] K. Kočí, M. Reli, I. Troppová, M. Sihor, J. Kupková, P. Kustrowski, P. Praus, Photocatalytic decomposition of N_2O over TiO_2/g-C_3N_4 photocatalysts heterojunction, Appl. Surf. Sci. 396 (2017) 1685-1695. https://doi.org/10.1016/j.apsusc.2016.11.242

[50] I. Krivtsov, E. García-Lopez, L. G.Marcì, Palmisano, Z. Amghouz, J. Gracía, S. Ordónez, E. Díaz, Selective photocatalytic oxidation of 5-hydroxymethyl-2-furfural to 2,5-furandicarboxyaldehyde in aqueous suspension of g-C_3N_4, Appl. Catal. B 204 (2017) 430-439. https://doi.org/10.1016/j.apcatb.2016.11.049

[51] H. Liu, D. Chen, Z. Wang, H. Jing, R. Zhang, Microwave-assisted molten-salt rapid synthesis of isotype triazine-/heptazine based g-C_3N_4 heterojunctions with highly enhanced photocatalytic hydrogen evolution performance, Appl. Catal. B 203 (2017) 300-313. https://doi.org/10.1016/j.apcatb.2016.10.014

[52] I. Papailias, T. Giannakopoulou, N. Todorova, D. Demotikali, J. Yu, C. Trapalis, Photocatalytic activity of modified g-C_3N_4/TiO_2 nanocomposites for NOx removal, Catal. Today 280 (2017) 37-44. https://doi.org/10.1016/j.cattod.2016.06.032

[53] S. Samanta, S. Khilari, D. Pradhan, R. Srivastava, An efficient, visible light driven, selective oxidation of aromatic alcohols and amines with O_2 using $BiVO_4$/g-C_3N_4 nanocomposite: A systematic and comprehensive study toward the development of a photocatalytic process, ACS Sustainable Chem. Eng. 5 (2017) 2562-2577. https://doi.org/10.1021/acssuschemeng.6b02902

[54] J. Shi, C. Cheng, Y. Hu, M. Liu, L. Guo, One-pot preparation of porous Cr_2O_3/g-C_3N_4 composites towards enhanced photocatalytic H_2 evolution under visible-light irradiation, Int. J. Hydrogen Energy 42 (2017) 4651-4659. https://doi.org/10.1016/j.ijhydene.2016.07.030

[55] S. Tan, Z. Xing , J. Zhang, Z. Li, X. Wu, J. Cui, J. Kuang, J. Yin, W. Zhou, Meso-g-C_3N_4/g-C_3N_4 nanosheets laminated homojunctions as efficient visible-light-driven photocatalysts, Int J Hydrog Energy 42 (2017 25969-25979. https://doi.org/10.1016/j.ijhydene.2017.08.202

[56] W. Xing, C. Li, G. Chen, Z. Han, Y. Zhou, Y. Hu, Q. Meng, Incorporating a novel metal-free interlayer into g-C_3N_4 framework for efficiency enhanced photocatalytic H_2 evolution activity, Appl. Catal. B, 203 (2017) 65-71. https://doi.org/10.1016/j.apcatb.2016.09.075

[57] D.B. Hernández-Uresti, A. Vázquez, D. Sanchez-Martinez, S. Obrégon, Performance of the polymeric g-C_3N_4 photocatalyst through the degradation of pharmaceutical pollutants under UV–vis irradiation, J. Photochem. Photobiol. A Chem. 324 (2016) 47-52. https://doi.org/10.1016/j.jphotochem.2016.01.031

[58] X. Liu, H. Qin, W. Fan, Enhanced visible-light photocatalytic activity of a g-C_3N_4/m-$LaVO_4$ heterojunction: band offset determination, Sci. Bull. 61 (2016) 645-655. https://doi.org/10.1007/s11434-016-1053-7

[59] J. Ma, C. Wang, H. He, Enhanced photocatalytic oxidation of no over g-C_3N_4-TiO_2 under UV and visible light, Appl. Catal. B 184 (2016) 28-34. https://doi.org/10.1016/j.apcatb.2015.11.013

[60] A. Qu, X. Xu, H. Xie, Y. Zhang, Y. Li, J. Wang, Effects of calcining temperature on photocatalysis of g-C_3N_4/TiO_2 composites for hydrogen evolution from water, Mater. Res. Bull. 80 (2016) 167-344. https://doi.org/10.1016/j.materresbull.2016.03.043

[61] W. Shan, Y. Hu, Z. Bai, M. Zheng, C. Wei, In situ preparation of g-C_3N_4/bismuth-based oxide nanocomposites with enhanced photocatalytic activity, Appl. Catal. B, 188 (2016) 1-12. https://doi.org/10.1016/j.apcatb.2016.01.058

[62] L. Wang, M. Yu, C. Wu, N. Deng, C. Wang, X. Yao, Synthesis of Ag/g-C_3N_4 composite as highly efficient visible-light photocatalyst for oxidative amidation of aromatic aldehydes, Adv. Synth. Catal. 358 (2016) 2631-2641. https://doi.org/10.1002/adsc.201600138

[63] J. Zou, L. Wang, J. Nie, Q. Xing, X. Luo, H. Du, S. Luo, S. Suib, Synthesis and efficient visible light photocatalytic H_2 evolution of a metal-free g-C_3N_4/graphene quantum dots hybrid photocatalyst, Appl. Catal. B 193 (2016) 103-109. https://doi.org/10.1016/j.apcatb.2016.04.017

[64] W. Ho, Z. Zhang, M. Xu, X. Zhang, X. Wang, Enhanced visible-light-driven photocatalytic removal of NO: effect on layer distortion on g-C_3N_4 by H_2 heating, Appl. Catal. B 179 (2016) 106-112. https://doi.org/10.1016/j.apcatb.2015.05.010

[65] L. Cui, Y. Liu, X. Fang, C. Yin, S. Li, D. Sun, S. Kang, Scalable and clean exfoliation of graphitic carbon nitride in NaClO solution: enriched surface active sites for enhanced photocatalytic H_2 evolution, Green Chemistry 20 (2018) 1354-1361. https://doi.org/10.1039/C7GC03704J

[66] B. Chai, J. Yan, G. Fan, G. Song, In situ fabrication of $CdMoO_4$/g-C_3N_4 composites with improved charge separation and photocatalytic activity under visible light irradiation, Chinese J. of Catal. 41 (2020) 170-179. https://doi.org/10.1016/S1872-2067(19)63383-8

[67] D. Sun, Y. Zhang, Y. Liu, Z. Wang, X. Chen, Z. Meng, S. Kang, Y. Zheng, L. Cui, M. Chen, M. Dong, B. Hu, In-situ homodispersely immobilization of Ag@AgCl on chloridized g-C_3N_4 nanosheets as an ultrastable plasmonic photocatalyst, Chem. Eng. J. 384 (2020) 123259. https://doi.org/10.1016/j.cej.2019.123259

[68] S. Kang, M. He, M. Chen, Y. Liu, Y. Wang, Y. Wang, M. Dong, X. Chang, L. Cui, Surface amino group regulation and structural engineering of graphitic carbon nitride with enhanced photocatalytic activity by ultrafast ammonia plasma immersion modification, ACS Appl. Mater. Inter. 11 (2019) 14952-14959. https://doi.org/10.1021/acsami.9b01068

[69] Mason, T., Lorimer, J. (2003). Applied sonochemistry: uses of power ultrasound in chemistry and processing. Weinheim: Wiley.

[70] M. Dickman, M. Pope, Peroxo and superoxo complexes of chromium, molybdenum, and tungsten, Chem. Rev. 94 (1994) 569-584. https://doi.org/10.1021/cr00027a002

[71] H. Nakajima, T. Kudo, Reaction of metal, carbide, and nitride of tungsten with hydrogen peroxide characterizes by 183 W nuclear magnetic resonance and raman spectroscopy, Chem. Mater. 11 (1999) 691-697. https://doi.org/10.1021/cm980544o

[72] J. Xu, L. Zhang, R. Shi, Y. Zhu, Chemical exfoliation of graphitic carbon nitride for efficient heterogeneous photocatalysis, J. Mater. Chem. A 1 (2013) 14766-14772. https://doi.org/10.1039/C3TA13188B

[73] T. Ma, Y. Tang, S. Dai, S. Qiao, Proton-functionalized two-dimensional graphitic carbon nitride nanosheet: an excellent metal-/label-free biosensing platform, Small 10 (2014) 2382–2389. https://doi.org/10.1002/smll.201303827

[74] S. Kang, M. He, M. Chen, J. Wang, L. Zheng, X. Chang, H. Duan, D. Sun, M. Dong, L. Cui, Ultrafast plasma immersion strategy for rational modulation of oxygen-containing and amino groups in graphitic carbon nitride, Carbon 159 (2020) 51-64. https://doi.org/10.1016/j.carbon.2019.12.022

[75] G. Bamwenda, H. Arakawa, The visible light induced photocatalytic activity of tungsten trioxide powders, Appl Cat A 210 (2001) 181–191. https://doi.org/10.1016/S0926-860X(00)00796-1

[76] E. Luévano-Hipólito, M. Cruz, Q. Yu, H. Brouwers, Precipitation synthesis of WO_3 for NOx removal using PEG as template, Ceram. Int. 40 (2014) 12123–12128. https://doi.org/10.1016/j.ceramint.2014.04.052

[77] G. Greczynski, L. Hultman, X-ray photoelectron spectroscopy: Towards reliable binding energy referencing, Prog. Mat. Sci. 107 (2020) 100591. https://doi.org/10.1016/j.pmatsci.2019.100591

[78] B. Zhu, P. Xia, Y. Li, W. Ho, J. Yu, Fabrication and photocatalytic activity enhanced mechanism of direct Z-scheme g-C_3N_4/Ag_2WO_4 photocatalyst, Appl. Surf. Sci. 391 (2017) 175-183. https://doi.org/10.1016/j.apsusc.2016.07.104

[79] J. Mao, T. Peng, X. Zhang, K. Li, L. Ye, L. Zan, Effect of graphitic carbon nitride microstructures on the activity and selectivity of photocatalytic CO_2 reduction under visible light, Catal. Sci. Technol. 3 (2013) 1253-1260. https://doi.org/10.1039/C3CY20822B

[80] F. Dong, Z. Zhao, T. Xiong, Z. Ni, W. Zhang, Y. Sun, W. K. Ho, In situ construction of g-C_3N_4/g-C_3N_4 metal-free heterojunction for enhanced visible-light photocatalysis, ACS Appl. Mater. Interfaces 5 (2013) 11392-11401. https://doi.org/10.1021/am403653a

[81] D.J. Miller, M.C. Biesinger, N.S. McIntyre, Interactions of CO_2 and CO at fractional atmosphere pressures with iron and iron oxide surfaces: one possible mechanism for surface contamination?, Surf. Interface Anal. 33 (2002) 299. https://doi.org/10.1002/sia.1188

[82] X. Lu, K. Xu, P. Chen, K. Jia, S. Liu, C. Wu, J. Facile one step method realizing scalable production of g-C_3N_4 nanosheets and study of their photocatalytic H_2 evolution activity, Mater. Chem. A2 (2014) 18924-18928. https://doi.org/10.1039/C4TA04487H

[83] N. Boonprakob, N. Wetchakun, S. Phanichphant, D. Waxler, P. Sherrell, A. Nattestad, J. Chen, B. Inceesungvorn, Enhanced visible-light photocatalytic activity of g-C_3N_4/TiO_2 films, J. Colloid Interf. Sci. 417 (2014) 402-409. https://doi.org/10.1016/j.jcis.2013.11.072

[84] F. Dong, Y. Sun, L. Wu, M. Fu, Z. Wu, Facile transformation of low cost thiourea into nitrogen-rich graphitic carbon nitride nanocatalyst with high visible light photocatalytic performance, Catal. Sci. Technol. 2 (2012) 1332-1335. https://doi.org/10.1039/c2cy20049j

[85] A.S. Lim, A. Atrens, ESCA studies of nitrogen-containing stainless steels, Appl. Phys. A 51 (1990) 411-418. https://doi.org/10.1007/BF00348382

[86] F. Zhan, J. Li, W. Li, Y. Liu, R. Xie, Y. Yang, Y. Li, Q. Chen, In situ formation of $CuWO_4$/WO_3 heterojunction plates array films with enhanced photoelectrochemical properties, Int. J. Hydrogen Energy 40 (2015) 6512-6520. https://doi.org/10.1016/j.ijhydene.2015.03.131

[87] Y.D. Premchand, S.A. Suthanthiraraj, Structural investigation of $(CuI)_{0.45}$–$(Ag_2WO_4)_{0.55}$ solid electrolyte using X-ray photoelectron and laser Raman spectroscopies, Electrochem. Commun. 6 (2004) 1266-1269. https://doi.org/10.1016/j.elecom.2004.09.026

[88] M. Mousavi, A. Habibi-Yangjeh, M. Abitorabi, Fabrication of novel magnetically separable nanocomposites using graphitic carbon nitride, silver phosphate and silver chloride and their applications in photocatalytic removal of different pollutants using visible-light irradiation, J. Colloid Interface Sci. 480 (2016) 218-231. https://doi.org/10.1016/j.jcis.2016.07.021

[89] Y. Cheng, L. He, G. Xia, C. Ren, Z. Wang, Nanostructured g-C_3N_4/AgI composites assembled by AgI nanoparticles-decorated g-C_3N_4 nanosheets for effective and mild photooxidation reaction, New J. Chem. 43 (2019) 14841-14852. https://doi.org/10.1039/C9NJ02725D

[90] J. Ke, H. Zhou, J. Liu, X. Duan, H. Zhang, S. Liu, S. Wang, Crystal transformation of 2D tungstic acid H_2WO_4 to WO_3 for enhanced photocatalytic water oxidation, J. Colloid Interface Sci. 514 (2018) 576-583. https://doi.org/10.1016/j.jcis.2017.12.066

[91] H. Xu, Z. Wu, Y. Wang, C. Lin, Enhanced visible-light photocatalytic activity from graphene-like boron nitride anchored on graphitic carbon nitride sheets, J. Mater. Sci. 52 (2017) 9477-9490. https://doi.org/10.1007/s10853-017-1167-6

[92] O. Legrini, E. Oliveros, A. Braun, Photochemical processes for water treatment, Chemical Reviews 93 (1993) 671-698. https://doi.org/10.1021/cr00018a003

[93] W. Teoh, J. Scott, R. Amal, Progress in heterogeneous photocatalysis: from classical radical chemistry to engineering nanomaterials and solar reactors, J. Phys. Chem. Lett. 3 (2012) 629-639. https://doi.org/10.1021/jz3000646

[94] T. Tachikawa, M. Fujitsuka, T. Majima, Mechanistic insight into the TiO_2 photocatalytic reactions: design of new photocatalysts, J. Phys. Chem. C 111 (2007) 5259-5275. https://doi.org/10.1021/jp069005u

[95] Y. Wang, Y. Wang, L. Yu, J. Wang, B. Du, X. Zhang, Enhanced catalytic activity of templated-double perovskite with 3D network structure for salicylic acid degradation under microwave irradiation: Insight into the catalytic mechanism, Chem. Eng. J. 368 (2019) 115-128. https://doi.org/10.1016/j.cej.2019.02.174

[96] J. Liqiang, Y. Qu, W. Baiqi, L. Shudan, J. Baojiang, Y. Libin, S. Jiazhong, Review of photoluminescence performance of nano-sized semiconductor materials and its relationships with photocatalytic activity, Sol. Energy Mater. Sol. Cells 90 (2006) 1773-1778. https://doi.org/10.1016/j.solmat.2005.11.007

[97] H. Katsumata, Y. Tachi, T. Suzuki, S. Kaneco, Z-scheme photocatalytic hydrogen production over WO_3/g-C_3N_4 composite photocatalysts, RSC Adv. 41 (2014) 21405-21409. https://doi.org/10.1039/C4RA02511C

[98] K. Alam, P. Kumar, P. Kar, U. Thakur, S. Zeng, K. Cui, K. Shankar, Enhanced charge separation in g-C_3N_4–BiOI heterostructures for visible light driven photoelectrochemical water splitting, Nanoscale Adv. 1 (2019) 1460-1471. https://doi.org/10.1039/C8NA00264A

[99] B. Chai, C. Liu, J. Yan, Z. Ren, In-situ synthesis of WO_3 nanoplates anchored on g-C_3N_4 Z-scheme photocatalysts for significantly enhanced photocatalytic activity, App. Surf. Sci. 448 (2018) 1-8. https://doi.org/10.1016/j.apsusc.2018.04.116

[100] L. Cui, X. Ding, Y. Wang, H. Shi, L. Huang, Y. Zuo, S. Kang, Facile preparation of Z-scheme WO_3/g-C_3N_4 composite photocatalyst with enhanced photocatalytic performance under visible light, App. Surf. Sci. 391 (2017) 202-210. https://doi.org/10.1016/j.apsusc.2016.07.055